Deformation and orientation effects in the decay of ^{268}Sg* formed in a ^{30}Si-induced reaction across the Coulomb barrier

Kirandeep Sandhu,[1] Manoj K. Sharma,[1,*] and Raj K. Gupta[2]
[1]*School of Physics and Materials Science, Thapar University, Patiala - 147004, Panjab, India*
[2]*Department of Physics, Panjab University, Chandigarh - 160014, India*
(Received 13 October 2012; published 26 December 2012)

The dynamical cluster decay model (DCM) is used to study the decay of the ^{268}Sg* compound nucleus formed in the ^{30}Si + ^{238}U reaction at above and below the Coulomb barrier energies. The neutron evaporation residues and fission cross sections are calculated in reference to the available data, including β_{2i}-static deformations with 'optimum' orientations. The role of spherical and the β_{2i}-dynamic deformed choices of fragmentation are also studied explicitly at the highest 169 MeV energy. The fission fragment distribution is symmetric at above-barrier energies, where equatorial collisions are preferred, but becomes asymmetric when the nuclei approach in pole-to-pole configuration at sub-barrier energies. Therefore, at above-barrier energies the calculations are carried out by considering 'hot fusion', equatorial collisions, whereas at sub-barrier energies the 'cold fusion', polar configuration is considered. The asymmetric peaks at sub-barrier energies may be associated with some competing process, like quasifission. The analysis of polar and equatorial configurations suggests that larger barrier modification is required at sub-barrier energies for neutron evaporation residue and fission fragments, i.e., the contribution of barrier modification at sub-barrier energies is relatively higher for a cold elongated polar configuration as compared to a hot compact equatorial configuration. Finally, the potential energies surfaces for the Si-induced reaction are compared with the *S*-induced reaction on the ^{238}U target, at comparable center of mass energies.

DOI: 10.1103/PhysRevC.86.064611 PACS number(s): 25.70.Jj, 24.10.−i, 25.60.Pj, 27.90.+b

I. INTRODUCTION

The stable superheavy nuclear systems can be synthesized by making use of highly asymmetric hot fusion reactions in which ^{238}U, ^{242,244}Pu, ^{243}Am, ^{245,248}Cm, ^{249}Bk, and ^{249}Cf actinide targets are collided with the doubly magic ^{48}Ca projectile. The above-mentioned actinide targets are usually prolate deformed nuclei, hence there exists a possibility that the projectile hits the equatorial orientation of the deformed target nucleus and thus form a most compact starting configuration on way to the compound nucleus formation/decay [1–3]. This process is more viable at energies higher than the Coulomb barrier. Such reactions have relatively higher fusion probability, compared to the reactions using spherical beams such as Pb and Bi with Ca to Cr targets in the so-called cold fusion reactions. Hence, the use of actinide targets is essential to achieve the maximum neutron excess and to attain the most compact configuration, required for higher fusion probability. Therefore, the hot fusion reactions have been extensively used as a tool for understanding the dynamics of superheavy elements. The situation changes drastically when the energy is decreased to the sub-barrier region. The cross sections drop rapidly in this region as the interactions are limited to polar collisions where the reseparation of the reaction partners is relatively large (elongated configurations) [1–3]. Intuitively, it seems reasonable that the former configuration would more likely result in fusion-fission, and the later in quasifission.

In the context of the above discussion, one may conclude that the energy of the compound system, along with deformations and orientations of projectile and target nuclei, plays an extremely important role in understanding the dynamics of heavy and superheavy nuclei. In fact, a thorough knowledge of the orientation degree of freedom may impart useful information regarding the understanding of phenomena like fusion-hinderance and fusion-suppression, which are favored at extreme sub-barrier and above-barrier energies, respectively.

In the present work, we have studied the decay of compound nucleus ^{268}Sg* formed in the ^{30}Si induced reaction on ^{238}U, using the dynamical cluster decay model (DCM) [4–14]. The calculations are made in reference to the experimental data of [15], using in the DCM the quadrupole deformations with optimum orientations, considering the ^{30}Si + ^{238}U → ^{268}Sg* as the hot fusion reaction. In terms of the orientation degrees of freedom, for the hot fusion reactions at above-barrier energies, the prolate deformed nuclei collide in equatorial configuration, whereas the same for cold fusion reactions at sub-barrier energies collide in polar configurations. Hence, the role of 'noncompact' (equivalently, elongated) polar collisions are explicitly studied for the sub-barrier region in terms of a cold fusion reaction in the DCM framework. In DCM, the optimum orientations are given for polar, elongated and equatorial, compact, respectively, for fusion configurations corresponding to the largest interaction radius with lowest barrier and smallest interaction radius with highest barrier.

First, the neutron evaporation residue ($3n$, $4n$, and $5n$) cross sections are calculated at three different center-of-mass energies 128, 133, and 144 MeV, respectively, and then fission cross sections at a wide range of $E_{\text{c.m.}} = 125$ MeV to 169 MeV energies by considering equatorial collisions. The role of polar collisions is also worked out at the sub-barrier energy region.

*msharma@thapar.edu

Strong variations in the mass distribution are observed while going from the above-barrier energy region to the sub-barrier energy region. Specifically, a symmetric mass distribution is observed for the hot equatorial collisions, which becomes asymmetric with the inclusion of polar collision at sub-barrier energies.

Our present calculations are based on the proton magic $Z = 120$ and neutron magic $N = 184$ for the fitting of neutron evaporation and fission cross sections, because other recent calculations [4] based on DCM show that $Z = 120$ and $N = 184$ are the best possible choices for the proton and neutron magic pairs in the superheavy mass region.

The paper is organized as follows. Section II gives a brief account of the dynamical cluster decay model, extended to include the deformations and orientation effects of the incoming and outgoing fragments. The calculations and discussions are presented in Sec. III. Finally the results are summarized in Sec. IV.

II. THE DYNAMICAL CLUSTER DECAY MODEL (DCM)

The DCM [4–14], based on the quantum mechanical fragmentation theory (QMFT) [16–18], is worked out in terms of the collective coordinates of mass (and charge) asymmetries $\eta = (A_1 - A_2)/(A_1 + A_2)$ [and $\eta_Z = (Z_1 - Z_2)/(Z_1 + Z_2)$], and the relative separation R. These two coordinates refer, respectively, to the nucleon-division (or -exchange) between the outgoing fragments, and the transfer of kinetic energy of incident channel to internal excitation [total excitation energy (TXE) or total kinetic energy (TKE)] of the outgoing channel. In terms of these co-ordinates, using partial waves analysis, the compound nucleus decay cross section is given as

$$\sigma = \sum_{\ell=0}^{\ell_{\max}} \sigma_\ell = \frac{\pi}{k^2} \sum_{\ell=0}^{\ell_{\max}} (2\ell + 1) P_0 P; \quad k = \sqrt{\frac{2\mu E_{\text{c.m.}}}{\hbar^2}}. \tag{1}$$

The preformation probability P_0 refers to η motion and the penetrability P to R motion, both depending on angular momentum ℓ and temperature T. In Eq. (1), μ $(=\frac{A_1 A_2}{A_1 + A_2} m)$ is the reduced mass, with m as the nucleon mass. $\ell_{\max}$ is the maximum angular momentum, fixed for the vanishing of the light particles (here, only neutrons) cross section, i.e., σ_{ER} $(=\sigma_{xn}, x = 3 \text{ or } 4 \text{ or } 5)$ becoming negligibly small at $\ell = \ell_{\max}$.

The P_0 imparts important information regarding the structural aspects of the decaying nucleus and is calculated by solving the stationary Schrödinger equation in η, at a fixed value of $R = R_a$,

$$\left\{ -\frac{\hbar^2}{2\sqrt{B_{\eta\eta}}} \frac{\partial}{\partial \eta} \frac{1}{\sqrt{B_{\eta\eta}}} \frac{\partial}{\partial \eta} + V(\eta, R, T) \right\} \psi^\nu(\eta) = E^\nu \psi^\nu(\eta), \tag{2}$$

with $\nu = 0, 1, 2, 3 \ldots$ referring to ground-state $(\nu = 0)$ and excited-states solutions, with the ground state P_0 given as

$$P_0 = |\psi(\eta(A_i))|^2 \sqrt{B_{\eta\eta}} \frac{2}{A_{CN}}, \tag{3}$$

and for a Boltzmann-like function,

$$|\psi|^2 = \sum_{\nu=0}^{\infty} |\psi^\nu|^2 \exp(-E^\nu/T). \tag{4}$$

The mass parameters $B_{\eta\eta}$ used in Eq. (2) are the smooth hydrodynamical masses [19] and the fragmentation potential $V_R(\eta, T)$, that goes in the Schrödinger equation (2), is defined as

$$\begin{aligned} V_R(\eta, T) = & \sum_{i=1}^{2} [V_{\text{LDM}}(A_i, Z_i, T)] \\ & + \sum_{i=1}^{2} [\delta U_i] \exp\left(-T^2/T_0^2\right) \\ & + V_C(R, Z_i, \beta_{\lambda i}, \theta_i, T) + V_P(R, A_i, \beta_{\lambda i}, \theta_i, T) \\ & + V_\ell(R, A_i, \beta_{\lambda i}, \theta_i, T), \end{aligned} \tag{5}$$

where V_{LDM} and δU are, respectively, the T-dependent liquid drop and shell correction energies, taken from Refs. [20,21], i.e., the total binding energy in DCM is defined as $B_{\exp} = V_{\text{LDM}}(T = 0) + \delta U(T = 0)$ with shell corrections estimated by using the 'empirical' formula of Myers and Swiatecki [21]. Apparently, it would have been more realistic to obtain the shell corrections δU from the shell model, instead of the phenomenological Myers-Swiatecki formula. However, we refit [22–24] the constants of V_{LDM} to get the experimental ground-state binding energies $B_{\exp}$ within <1.5 MeV. In other words, we essentially use the experimental binding energies. Whenever the $B_{\exp}$ were not available, the theoretical estimates of Möller *et al.* [25] are used. The T dependence of the constants of the refitted V_{LDM} are taken from Fig. 1 of Davidson *et al.* [20].

The V_C, V_P, and V_ℓ are, respectively, the T-dependent Coulomb potential, the nuclear proximity potential, and the centrifugal potential, with the moment of inertia taken in the complete sticking limit. The Coulomb potential for deformed

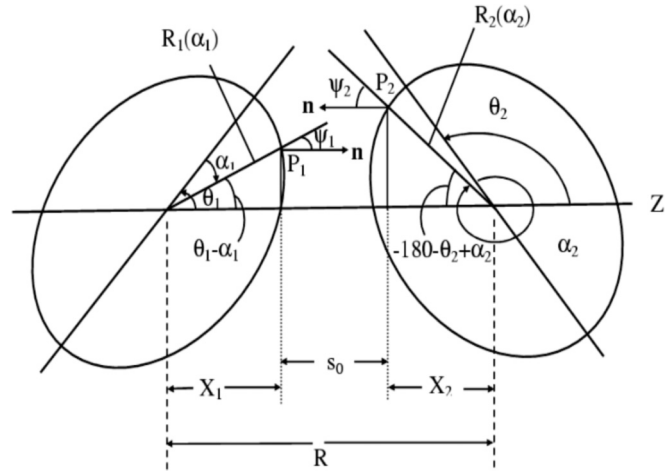

FIG. 1. Systematic configuration of any two axially symmetric, deformed, oriented nuclei, lying in the same plane, taken from [1].

and oriented nuclei is given by

$$V_C(R, Z_i, \beta_{\lambda i}, \theta_i, T) = Z_1 Z_2 e^2/R(T) + 3Z_1 Z_2 e^2 \times \sum_{\lambda,i=1,2} \frac{R_i^{\lambda}(\alpha_i, T)}{(2\lambda+1)R(T)^{\lambda+1}} \times Y_{\lambda}^{(0)}(\theta_i) \times \left[\beta_{\lambda i} + \frac{4}{7}\beta_{\lambda i}^2 Y_{\lambda}^{(0)}(\theta_i)\right], \quad (6)$$

where $Y_{\lambda}^{(0)}(\theta_i)$ are the spherical harmonics function. The centrifugal potential is given by

$$V_{\ell}(R, A_i, \beta_{\lambda i}, \theta_i, T) = \frac{\hbar^2 \ell(\ell+1)}{2I(T)} \quad (7)$$

with $I = I_S = \mu R^2 + \frac{2}{5}A_1 m {R_1}^2(\alpha_1, T) + \frac{2}{5}A_2 m {R_2}^2(\alpha_2, T)$, the moment of inertia in the sticking limit, or, alternatively, the one calculated in nonsticking limit, $I = I_{NS} = \mu R^2$. Note that I_{NS} corresponds to the supposition of prompt emission of fragments, used generally for the experimental determination of the $\ell_{\max}$ value.

The penetrability P in Eq. (1) is the WKB integral

$$P = \exp\left[-\frac{2}{\hbar}\int_{R_a}^{R_b}(2\mu\{V(R) - Q_{\text{eff}}\})^{1/2} dR\right] \quad (8)$$

with R_b as the second turning point satisfying

$$V(R_a, \ell) = V(R_b, \ell) = Q_{\text{eff}}(T, \ell) = \text{TKE}(T) \quad (9)$$

and R_a is given as

$$R_a = R_1(\alpha_1, T) + R_2(\alpha_2, T) + \Delta R(T) \quad (10)$$

and is the first turning point of the penetration path. The radius vectors $R_i(\alpha_i, T)$ is defined as

$$R_i(\alpha_i, T) = R_{0i}(T)\left[1 + \sum_{\lambda}\beta_{\lambda i} Y_{\lambda}^{(0)}(\alpha_i)\right], \quad (11)$$

where

$$R_{0i}(T) = \left[1.28A_i^{1/3} - 0.76 + 0.8A_i^{-1/3}\right](1 + 0.0007T^2) \quad (12)$$

and T (in MeV) is given by the center-of-mass energy $E_{\text{c.m.}}$ and the Q_{in} value of the incoming channel, since $E_{CN}^* = E_{\text{c.m.}} + Q_{in} = (A_{CN}/a)T^2 - T$ with the level density parameter $a =$ 9–11, depending on the mass A_{CN} of the compound nucleus. In the present calculations, we have taken $a = 11$. It is relevant to point out here that instead of using the reduced mass μ in the calculation of the WKB penetrability P in Eq. (8), one should in fact use the mass inertia B_{RR} (say, the cranking mass in the R co-ordinate) which is influenced by the geometry changes due to the configuration evolution. In fact, the average value of B_{RR} should be preferred as the mass parameter B_{RR} shows large fluctuations with the mass asymmetry parameter η. In reference to the work of [26], the averaged mass reads as

$$\overline{B_{RR}} = \frac{1}{\eta_f}\int_0^{\eta_f} B_{RR}(R, \eta) d\eta. \quad (13)$$

An order of magnitude for the difference introduced can be estimated by comparing the results of μ and average B_{RR} in Eq. (13), mentioned above (see, e.g., Fig. 2(a) in Ref. [26]). Also, according to the works of Refs. [26–28], the distance of closest approach ΔR is almost doubled and hence P gets lowered. However, in the DCM, ΔR is an empirically fitted parameter, so the use of reduced mass μ seems justified.

For deformations $\beta_{\lambda i}$, we use β_{2i} alone, taken from Ref. [25], and the orientations θ_i are the "optimum" orientations θ_i^{opt} of the "hot fusion" and "cold fusion" processes of [1]. For the hot fusion reaction, the barrier is highest and the interaction radius is smallest, which, for the compact case, occurs for the collisions in the direction of the minor axis of the deformed reaction partner, i.e., for 90° orientation, giving rise to equatorial configuration [2]. In a similar manner, the elongated configuration of reaction partners comes into picture, only when the barrier is lowered (and the interaction radius is highest) for 0° or 180° orientations of colliding nuclei [2] which can be further understood with the help of Fig. 1, taken from [1].

As it is already mentioned above, the static deformations in DCM are taken from the theoretical estimates of Möller and Nix [25], and the temperature dependence in the deformations are considered to enter from [29,30], and are given as

$$\beta_{\lambda i}(T) = \exp(-T/T_0)\beta_{\lambda i}(0), \quad (14)$$

where $\beta_{\lambda i}(0)$ are the static deformations and T_0 is the temperature of the nucleus at which shell effects start to vanish.

The neck-length parameter ΔR, defined in Eq. (10), is the relative separation distance between two fragments or clusters A_i and is shown to assimilate the neck formation effects [31–33]. The choice of ΔR for the best fit to the data allows us to define the effective "barrier lowering" [defined below in Eq. (15)] parameter $\Delta V_B(\ell)$ for each ℓ as the difference between the actually used barrier $V(R_a, \ell)$ and the top of the calculated barrier $V_B(\ell)$. The $\Delta V_B(\ell)$ can be read as

$$\Delta V_B(\ell) = V(R_a, \ell) - V_B(\ell). \quad (15)$$

Note that ΔV_B is defined as a negative quantity which means that the actually used barrier is effectively lowered, as explained in Fig. 2.

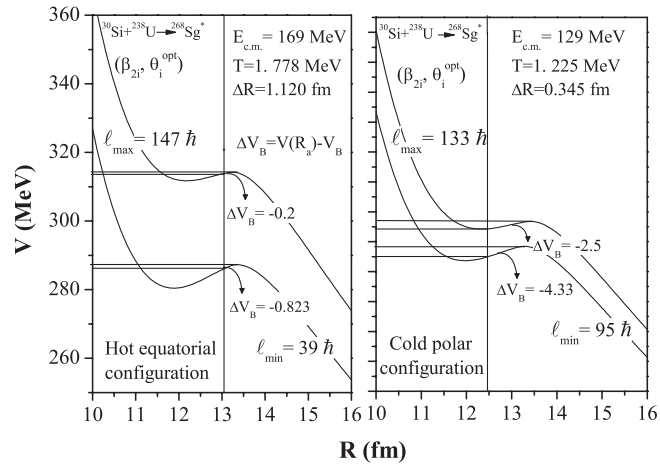

FIG. 2. Scattering potential for the decay of the $^{30}\text{Si} + ^{238}\text{U} \rightarrow ^{268}\text{Sg}^*$ reaction at two extreme ℓ values, the $\ell_{\max}$ and $\ell_{\min}$ for hot equatorial compact configuration and cold polar elongated configuration.

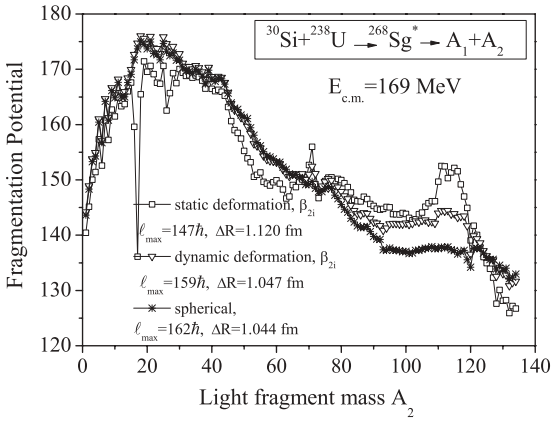

FIG. 3. Fragmentation potential for the $^{30}Si + ^{238}U \rightarrow ^{268}Sg^{*}$ reaction as a function of light mass fragment A_2 for spherical, static, and dynamical deformations β_{2i} with "optimum" orientations θ_i^{opt} at ℓ_{max} values.

III. CALCULATIONS AND DISCUSSION

The decay of compound nucleus $^{268}Sg^{*}$ has been studied over a wide range of center-of-mass energies $E_{c.m.} = 125$–169 MeV, where both the neutron evaporation residues ($3n$, $4n$, and $5n$) and fission cross sections are measured at below- and above-barrier energies [15], respectively. The main aim of this work was to investigate the role of deformations and orientations affecting the dynamics of the $^{30}Si + ^{238}U \rightarrow ^{268}Sg^{*}$ reaction. It is very important to study the role of deformations of interacting nuclei and decaying fragments because both the target and compound nuclei are prolate deformed, and the motivation behind the introduction of the orientation degree of freedom explicitly in the study of this reaction is to observe the drastically changed potential energy surfaces, from asymmetric to symmetric mass distribution, at below and above the Coulomb barrier, respectively. The measurements from heavy ion collision reactions reveal the asymmetric mass distribution of fragments at sub-barrier energies. The asymmetry arises due to the pole-to-pole interaction of reaction partners, which favors the formation of the noncompact, elongated nuclear

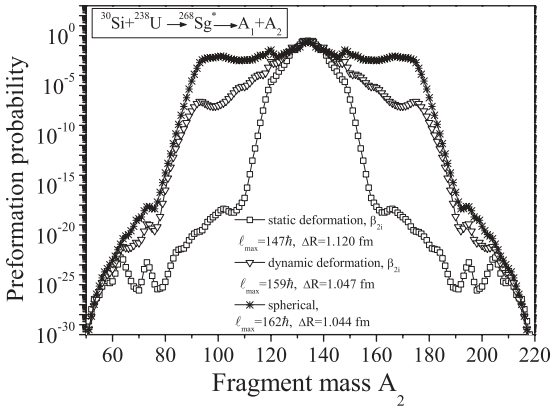

FIG. 4. Preformation probability P_0 for the $^{30}Si + ^{238}U \rightarrow ^{268}Sg^{*}$ reaction as a function of light mass fragment A_2 for spherical, static, and dynamical deformations β_{2i} with "optimum" orientations θ_i^{opt} at ℓ_{max} values.

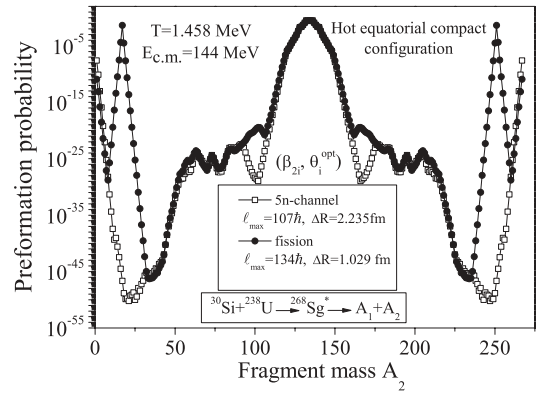

FIG. 5. Comparison of potential energy surfaces for $5n$ evaporation residue and symmetric fission of $^{268}Sg^{*}$, at $E_{c.m.} = 144$ MeV.

configuration, whereas a compact configuration is more suited for equatorial collisions at above barrier energies.

Following the experimental data [15], first we tried to fit the fission cross sections with spherical, β_{2i}-static, and with β_{2i}-dynamic choices of fragmentations within the framework of the DCM. The neutron evaporation residue ($3n$, $4n$, and $5n$) decay is discussed later in this section. The calculations are done by considering hot equatorial collisions leading to a compact configuration, which corresponds to the smallest interaction radius and highest potential barrier. The fragmentation potential $V(A_2)$, shown in Fig. 3, is plotted at the highest value of center-of-mass energy $E_{c.m.} = 169$ MeV and at $\ell = \ell_{max}$ for spherical, β_{2i}-static, and dynamical deformed configurations at optimum orientations. It can be seen from the Fig. 3 that the fragment's mass distribution remains nearly identical for light particles (LPs) and intermediate mass fragments (IMFs) but significant differences arise due to the inclusion of β_{2i}-static/dynamical deformations in potential energy surfaces for the fission region. A strong variation can be seen in the decaying path of β_{2i}-static choice of fragmentation, which otherwise remains smooth for the spherical choice of fragments. The β_{2i}-dynamic deformations exhibit an intermediate structural behavior. The occurrence of prominent minima in Fig. 3 (so also in Figs. 7, 11, and 12, which are discussed

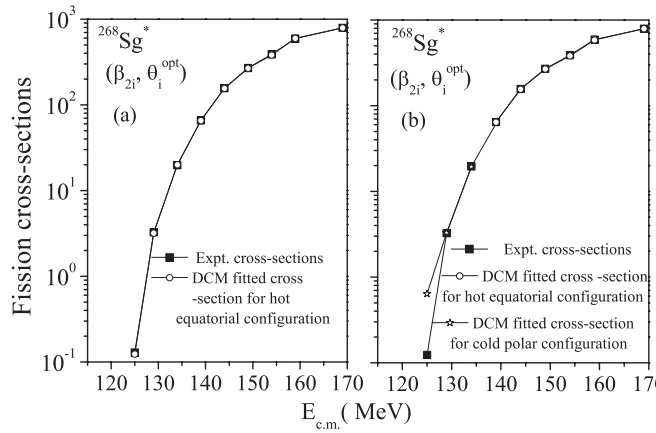

FIG. 6. DCM calculated fission cross sections for the decay of $^{268}Sg^{*}$ (in hot equatorial and cold polar configurations), plotted as the function of $E_{c.m.}$, compared with the experimental data of Ref. [15].

TABLE I. Experimental and DCM calculated evaporation residue cross sections σ_{xn}, $x = 3$, 4, and 5 in the decay of ^{268}Sg* formed in the ^{30}Si + ^{238}U reaction.

$E_{\text{c.m.}}$ (MeV)	xn	T (MeV)	$\ell_{\max}$ ($\hbar$)	ΔR (fm)	σ_{xn}^{DCM} (pb)	σ_{xn}^{exp} (pb)
128	3n	1.207	120	1.536	14.7	15 upper limit
133	4n	1.291	113	1.850	10.2	$10 \pm {}^{10}_{6}$
144	5n	1.458	107	2.235	66.2	$67 \pm {}^{67}_{37}$

later) at $A_2 = 17$ may be due to the inappropriate values of optimized β_2 deformations used in the calculations and occur mainly because of the proximity (V_P) part of the fragmentation potential. A similar trend can be seen in Fig. 4 where the preformation probability P_0 is plotted as a function of fragment mass A_2 by considering the nuclei as spherical, β_{2i}-static, and β_{2i}-dynamic deformed. It is relevant to mention here that the maximum preformation probability P_0 corresponds to minima in the fragmentation potential. Hence, Fig. 4 clearly shows the emergence of differences in the preformation probabilities in the same mass region $70 \leqslant A_2 \leqslant 130$, similar to the one observed in the case of the fragmentation plot (Fig. 3).

Another point of difference between spherical and deformed choices of fragmentations lies in the fact that in the case of the spherical choice, the dominating fragments contributing towards fission cross sections are lying in the mass range $(A/2) \pm 42$ while a comparatively lesser number of fragments are contributing towards fission with the inclusion of deformations (β_{2i} static and β_{2i} dynamic). The dominant fission fragments for dynamical deformations are $(A/2) \pm 14$ and for static deformations $(A/2) \pm 9$. Hence, this huge difference in the fission fragmentation can be seen in going from the spherical to deformed choice of fragmentation. Evidently, the β_{2i}-dynamic distribution lies in between that of the spherical and β_{2i}-static cases of fragmentation.

As mentioned above, in addition to experimental data on fission decay in the energy range $E_{\text{c.m.}} = 125$–169 MeV, neutron evaporation residue data are also available at three different energies $E_{\text{c.m.}} = 128$, 133, and 144 MeV, respectively, for 3n, 4n, and 5n evaporation products [15]. In view of this situation, we have fitted the neutron and fission cross sections independently as they are measured at different energies (only one energy is common, i.e., 144 MeV for the 5n decay and fission channel). It is of further interest to see the behavior of the potential energy surfaces corresponding to the fitting of neutron evaporation residues and fission cross sections. Figure 5 shows the plotted preformation probability P_0 as the function of fragment mass A_2 for the case of 5n decay and fission, respectively, at 144 MeV. It is clear from Fig. 5 that the two potential energy surfaces govern a similar behavior for the 5n channel (for ER) and the fission decay path, although the IMF region is quite differently preformed for the neutron evaporation channel and fission dynamics. Some points of differences, observed from Fig. 5, are (i) a relatively higher value of $\ell_{\max}$ is required to study the behavior of fission as compared to the neutron evaporation residue decay. (ii) 5n decay requires a higher value of neck-length parameter ΔR (=2.235 fm) than the symmetric fission, where fission fragments are decaying at the neck-length parameter of 1.029 fm. The different magnitudes of the neck-length parameter ΔR simply means that the two processes [neutron evaporation residues and fusion-fission (ff)] occur at different time-scales. The detailed description of neck-length parameter will be given later, in the following.

TABLE II. Experimental and DCM calculated fission cross sections σ_{fission} in the decay of ^{268}Sg* formed in the ^{30}Si + ^{238}U reaction by considering hot equatorial configuration.

$E_{\text{c.m.}}$(MeV)	T (MeV)	$\ell_{\max}$ ($\hbar$)	ΔR (fm)	$\sigma_{\text{fission}}^{\text{DCM}}$(mb)	$\sigma_{\text{fission}}^{\text{exp}}$(mb)
169	1.778	147	1.120	792	792
159	1.658	142	1.076	594	597
154	1.594	139	1.058	382	390
149	1.528	136	1.049	268	269
144	1.458	134	1.029	156	156.5
139	1.385	133	0.997	65.6	65.9
134	1.307	131	0.964	19.8	20.0
129	1.225	128	0.944	3.18	3.25
125	1.154	126	0.905	0.129	0.123

TABLE III. Experimental and DCM calculated fission cross sections σ_{fission} in the decay of ^{268}Sg* formed in the ^{30}Si + ^{238}U reaction by considering cold polar configuration.

$E_{\text{c.m.}}$(MeV)	T (MeV)	$\ell_{\max}$ ($\hbar$)	ΔR (fm)	$\sigma_{\text{fission}}^{\text{DCM}}$(mb)	$\sigma_{\text{fission}}^{\text{exp}}$(mb)
134	1.307	144	0.524	19.5	20.0
129	1.225	133	0.345	3.30	3.25
125	1.154	130	0.000	0.638	0.123

Using static deformations up to β_{2i}, and using hot compact equatorial configurations, we have calculated the fission and evaporation residue cross sections at above and below barrier energies in the framework of the DCM. Figure 6(a), along with the tabulated results of Tables I and II, clearly show a nice comparison of experimental and DCM fitted cross sections. The role of equatorial and polar orientations (hot and cold processes) is also worked out in the DCM. Actually,

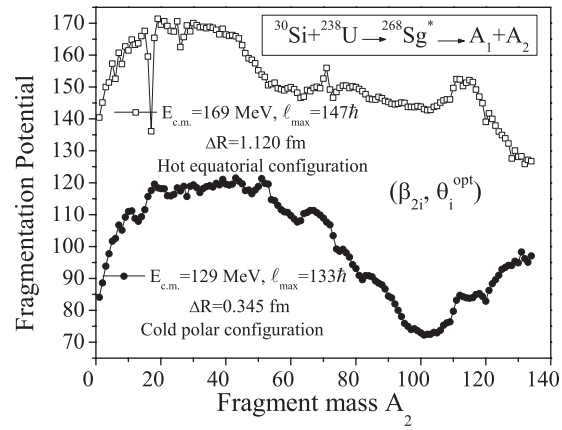

FIG. 7. Variation of fragmentation potential V (MeV) for the ^{30}Si + ^{238}U → ^{268}Sg* reaction as a function of light mass fragment A_2 for hot-compact and cold noncompact configurations.

the orientation degree of freedom plays an extremely important role since polar, noncompact, and equatorial, compact fusion configurations are obtained, respectively, corresponding to the largest interaction radius and lowest interaction barrier and the smallest interaction radius with highest interaction barrier. Following this prescription, further calculations are done by considering polar configurations at sub-barrier energies with $E_{\text{c.m.}} = 125$ to 134 MeV. In Fig. 6(a), the DCM-based calculated cross sections, using equatorial configurations, compare nicely with experimental data. The polar orientation based calculations at below the barrier region are shown in Fig. 6(b) and Table III. One may see that, with polar collisions, the DCM-based cross section at lowest energy is overestimated with respect to the experimental data. It might be due to the fact that with the polar configuration the barrier height decreases and hence cross sections are overestimated. In order to see the comparative effect of equatorial and polar orientations in nuclear dynamics, we have plotted in Fig. 7 the fragmentation potential as a function of fragment mass, which clearly shows a significant difference in the fragmentation paths of a hot compact configuration and cold noncompact configuration, respectively, at 169 MeV and 129 MeV. No change is observed in the LP's region while a significant change in the fragmentation behavior is observed for IMFs, heavy mass fragments (HMFs), and fission fragments which will be further clear from Fig. 8 where a detailed description of potential energy surfaces is represented. The fission mass distribution is plotted in Fig. 8, which shows the modified behavior of the potential energy surfaces at sub-barrier energies ($E_{\text{c.m.}} = 134$, 129, and 125 MeV). The

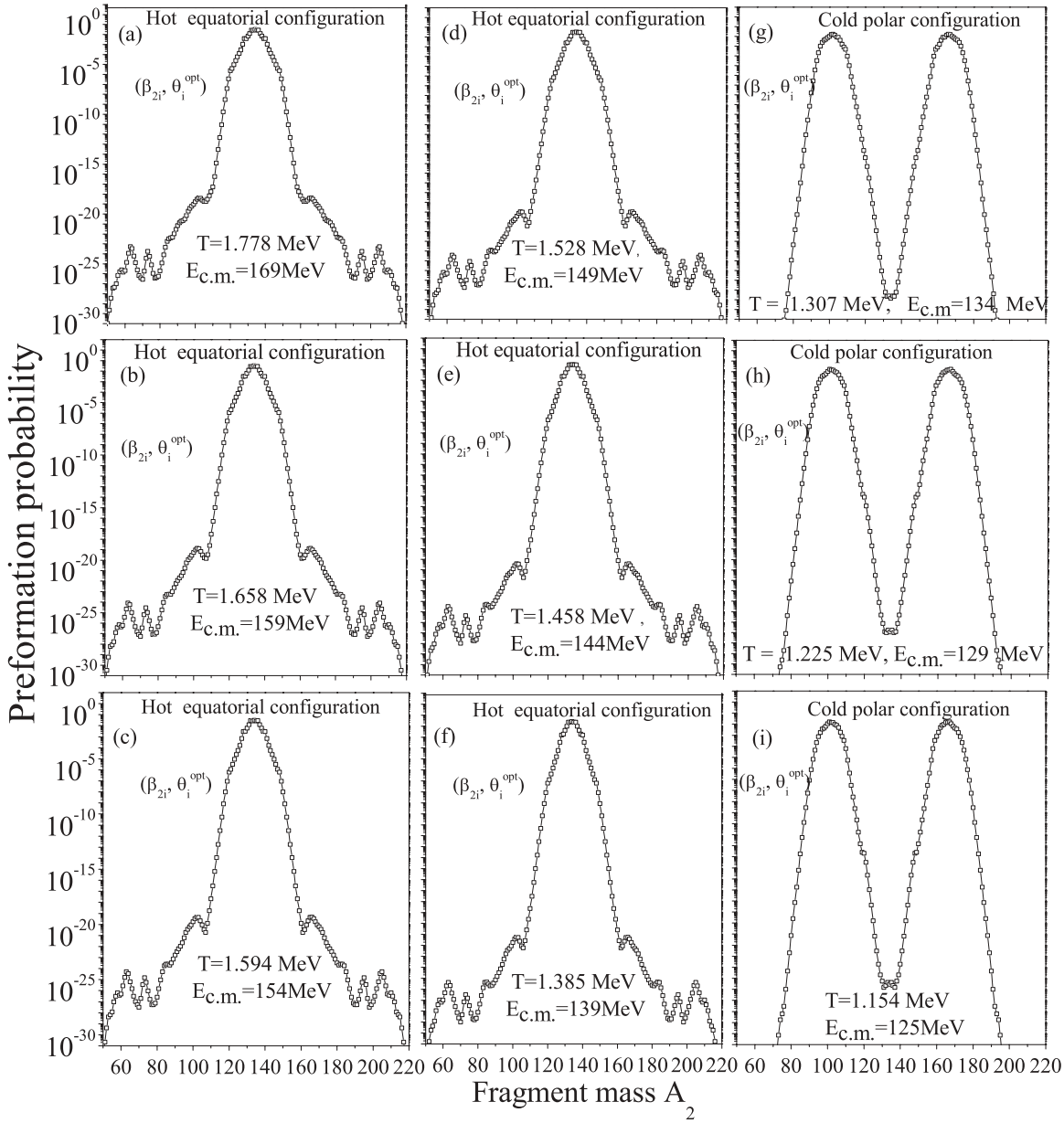

FIG. 8. Variation of preformation probability P_0 for the $^{30}\text{Si} + ^{238}\text{U} \rightarrow ^{268}\text{Sg}^*$ reaction as a function of light mass fragment A_2 at highest value of angular momentum $\ell_{\max}$ values, for the neck-length parameter ΔR fitted to the case of deformed nuclei.

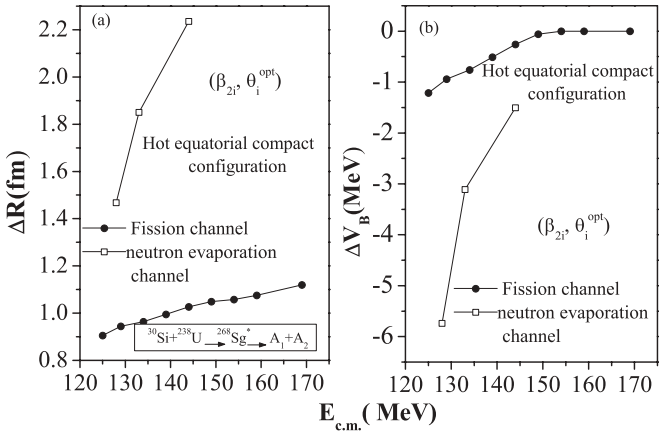

FIG. 9. The fitted neck-length parameter ΔR and calculated ΔV_B as a function of $E_{\text{c.m.}}$ for the decay of compound nucleus ^{268}Sg*.

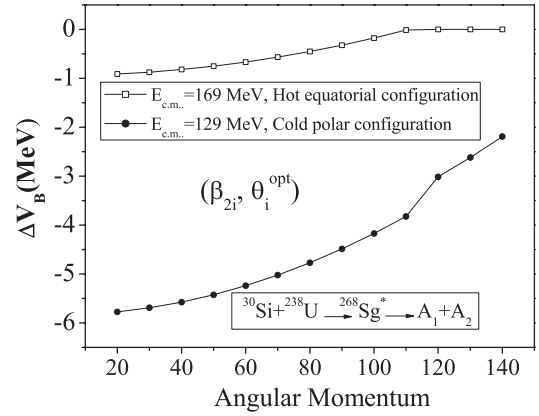

FIG. 10. Variation of ΔV_B as function of angular momentum ℓ for the decay of the compound nucleus ^{268}Sg*.

preformation probability remains symmetric for above barrier energies, represented in Figs. 8(a)–8(f) with $E_{\text{c.m.}} > 134$ MeV, where the projectile collides on equatorial sides of the target, but becomes dominantly asymmetric when nuclei collide pole-to-pole at sub-barrier energies shown in Figs. 8(g)–8(i). It is relevant to mention here that the asymmetric peaks are not due to any magic shell closures, it may arise due to some competing process like the quasifission process at near or below barrier energies.

The above observations may be associated with the results of Fig. 6(b) and Table III, where an enhancement in the fission cross section at deep sub-barrier energy $E_{\text{c.m.}} = 125$ MeV is reported. The enhancement in fission cross sections at a deep sub-barrier region indicate that fusion is not the main process after the projectile is captured inside the Coulomb barrier. Interestingly, we could not fit the evaporation residue cross sections in the sub-barrier region with polar orientations, and hence the possibility of some competing decay channel at the sub-barrier energy region seems justified.

We have taken different values of ΔR for neutron evaporation residues and fission decay calculations. Figure 9(a) shows the variation of ΔR as the function of $E_{\text{c.m.}}$ at all the energies ranging from 125 MeV to 169 MeV. It is clear from the figure that, for equatorial compact configuration, the magnitude of ΔR increases with increase in center-of-mass energies both for neutron evaporation residues and fission fragments. A similar increasing trend is observed for the polar noncompact configuration, but the magnitude of ΔR is much smaller than for equatorial collisions. The value of ΔR for the polar noncompact configuration is not shown in the graph, but tabulated in Table III. Moreover, the higher values of ΔR for neutron evaporation residues, as compared with ff in Fig. 9(a), means to suggest that the neutrons emission occurs earlier than symmetric fission.

The barrier lowering parameter ΔV_B is plotted in Fig. 9(b) as the function of $E_{\text{c.m.}}$. It is relevant to mention that the barrier lowering is an in-built property of the DCM which has the direct dependence on the value of neck-length parameter ΔR. This parameter shows its dominance at lower or at deep sub-barrier energies. The value of ΔV_B shows decrement in its value as the magnitude of $E_{\text{c.m.}}$ increases, which simply means that larger barrier lowering is needed for lower center-of-mass energies. We have also calculated the ΔV_B for the noncompact polar configuration (not shown here) which indicates that higher barrier modification is required for a noncompact configuration in the sub-barrier energy region. To explore this aspect further the barrier modification parameter ΔV_B is plotted in Fig. 10 as a function of angular momentum ℓ at two energies 169 and 129 MeV, respectively, for equatorial compact and polar noncompact configurations. As stated above, ΔV_B is much higher for the polar configuration than that for the equatorial one. Also, the ΔV_B seems to be of greater importance at lower ℓ- values, as its magnitude decreases with increase in angular momentum.

Figure 11 is plotted to see here the effects of angular momentum on barrier heights V_B as the function of fragment mass, which plays an important role for compact and noncompact configurations. It is clear from Fig. 11 that (i) the barrier-height increases for both the equatorial and polar configurations, respectively, at $E_{\text{c.m.}} = 169$ MeV and 129 MeV. The increasing behavior of V_B with fragment mass is the same as that for the heavier nuclear system like ^{215}Fr [7], and a just opposite behavior can be observed for the lighter nuclear system like ^{48}Cr [14] where the barrier height decreases with an increase in

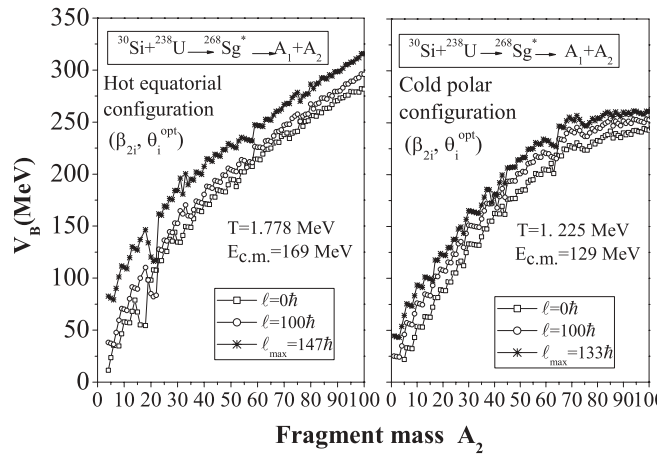

FIG. 11. Variation of V_B as function of A_2 for the decay of compound nucleus ^{268}Sg* at different values of ℓ.

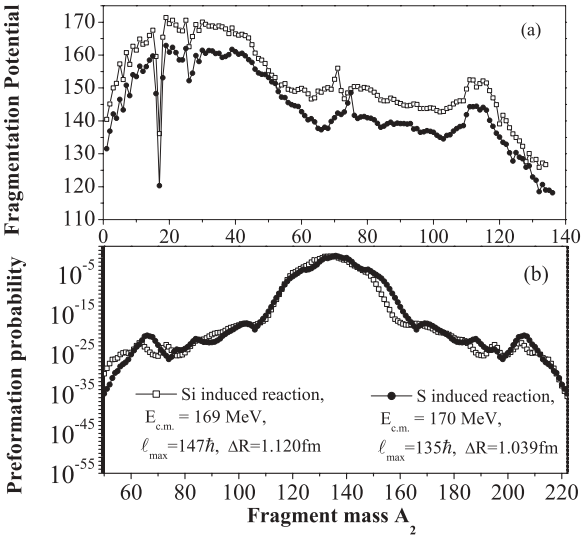

FIG. 12. Comparison of PES (fragmentation and preformation paths) for Si-induced and S-induced reactions, taking the same target (^{238}U) for both cases.

ℓ values. (ii) The magnitude of V_B is of smaller magnitude for polar noncompact configurations as compared to equatorial compact configurations, which signifies that barrier height decreases for the use of polar orientation.

Finally, the comparison between Si- and S-induced reactions, for keeping the target (^{238}U) same, is done at comparable energies, i.e., 169 MeV [15] and 170 MeV [34], respectively. From Figs. 12(a) and 12(b), we observe that fragmentation path and preformation probability are almost independent of projectile mass (^{30}Si or ^{34}S), although the neck-length parameter and angular momentum are smaller for the heavier projectile.

IV. SUMMARY

The fission and neutron evaporation residue cross sections for the reaction $^{30}\mathrm{Si} + ^{238}\mathrm{U} \rightarrow ^{268}\mathrm{Sg}^*$ are calculated by using the dynamical cluster decay model at both above and below barrier energies. The cross sections are calculated for β_{2i}-static deformations and 'optimum' orientation, considering the equatorial collisions of reaction partners leading to a compact compound nuclear system. The role of spherical and β_{2i}-dynamic deformations is also included to investigate the effect of deformations on the decay path of compound nucleus $^{268}\mathrm{Sg}^*$. Deformations show their influence particularly for the heavy mass fragments lying in the mass range $70 \leqslant A_2 \leqslant 130$. Therefore the deformation effects are of immense importance for studying dynamics of the $^{30}\mathrm{Si} + ^{238}\mathrm{U} \rightarrow ^{268}\mathrm{Sg}^*$ reaction. The role of cold fusion (polar collisions) are explicitly examined for the sub-barrier region. A variation in the mass distribution is observed from symmetric to asymmetric in going from the above barrier region to sub-barrier region, when equatorial collisions are supplemented by polar collisions for sub-barrier energies, which leads to the demonstration of the fact that quasifission may be competing with fission in the sub-barrier region. Other important results are (i) the barrier height V_B increases with increase in energy and angular momentum for both the configurations. (ii) Larger 'barrier modification' ΔV_B is needed for sub-barrier energies, i.e., relatively larger 'barrier modification' is required for a cold noncompact configuration as compared to hot compact configuration. (iii) The ΔV_B is reported to be least for the higher angular momentum states. (iv) Higher value of ΔR is required for neutron evaporation residues as compared to fission fragments. Finally, the comparison in Si-induced and S-induced reactions using the same target (^{238}U) at approximately the same energy reveals that PES remains identical for both the reactions, although higher values of neck-length parameter and angular momentum are preferred for the light mass projectile.

ACKNOWLEDGMENT

We are thankful to Council of Scientific and Industrial Research (CSIR), New Delhi, for support of this research work.

[1] R. K. Gupta, M. Balasubramaniam, R. Kumar, N. Singh, M. Manhas, and W. Greiner, J. Phys. G **31**, 631 (2005).
[2] R. K. Gupta, M. Manhas, and W. Greiner, Phys. Rev. C **73**, 054307 (2006).
[3] K. Nishio *et al.*, Eur. Phys. J. A **29**, 281 (2006).
[4] Niyti, R. K. Gupta, and W. Greiner, J. Phys. G **37**, 115103 (2010).
[5] R. K. Gupta, Niyti, M. Manhas, and W. Greiner, J. Phys. G **36**, 115105 (2009).
[6] R. K. Gupta and M. Bansal, Int. Rev. Phys. (I.RE.PHY.) **5**, 74 (2011).
[7] M. K. Sharma, G. Sawhney, R. K. Gupta, and W. Greiner, J. Phys. G **38**, 105101 (2011).
[8] M. K. Sharma, S. Kanwar, G. Sawhney, R. K. Gupta, and W. Greiner, J. Phys. G **38**, 055104 (2011); D. Jain, R. Kumar, M. K. Sharma, and R. K. Gupta, Phys. Rev. C **85**, 024615 (2012).
[9] R. K. Gupta, in *Lecture Notes in Physics 818*, *Clusters in Nuclei*, edited by C. Beck, Vol. I (Springer-Verlag, Berlin, Heidelberg, 2010), p. 223.
[10] R. K. Gupta, S. K. Arun, R. Kumar, and Niyti, Int. Rev. Phys. (I.RE.PHY.) **2**, 369 (2008).
[11] S. Kanwar, M. K. Sharma, B. B. Singh, R. K. Gupta, and W. Greiner, Int. J. Mod. Phys. E **18**, 1453 (2009).
[12] K. Sandhu, M. K. Sharma, and R. K. Gupta, Phys. Rev. C **85**, 024604 (2012).
[13] M. Kaur, R. Kumar, and M. K. Sharma, Phys. Rev. C **85**, 014609 (2012).
[14] B. B. Singh, M. K. Sharma, R. K. Gupta, and W. Greiner, Int. J. Mod. Phys. E **15**, 699 (2006).
[15] K. Nishio *et al.*, Phys. Rev. C **82**, 044604 (2010).
[16] J. Marhun and W. Greiner, Z. Phys. **251**, 431 (1972).

[17] R. K. Gupta and W. Greiner, in *Heavy Elements and Related New Phenomena*, edited by W. Greiner and R. K. Gupta, Vol. I (World Scientific, Singapore, 1999).
[18] M. K. Sharma, R. K. Gupta, and W. Scheid, J. Phys. G **26**, L45 (2000).
[19] H. Kröger and W. Scheid, J. Phys. G **6**, L85 (1980).
[20] N. J. Davidson, S. S. Hsiao, J. Markram, H. G. Miller, and Y. Tzeng, Nucl. Phys. A **570**, 61c (1994).
[21] W. Myers and W. J. Swiatecki, Nucl. Phys. **81**, 1 (1966).
[22] M. Balasubramaniam, R. Kumar, R. K. Gupta, C. Beck, and W. Scheid, J. Phys. G **29**, 2703 (2003).
[23] R. K. Gupta, R. Kumar, N. K. Dhiman, M. Balasubramaniam, W. Scheid, and C. Beck, Phys. Rev. C **68**, 014610 (2003).
[24] B. B. Singh, M. K. Sharma, and R. K. Gupta, Phys. Rev. C **77**, 054613 (2008).
[25] P. Möller, J. R. Nix, W. D. Myers, and W. J. Swiatecki, At. Data Nucl. Data Tables **59**, 185 (1995).
[26] R. K. Gupta, Phys. Rev. C **21**, 1278 (1980).
[27] S. Yamaji, K.-H. Ziegenhain, H. J. Fink, W. Greiner, and W. Scheid, J. Phys. G **3**, 1283 (1977).
[28] S. Yamaji, W. Scheid, H. J. Fink, and W. Greiner, Z. Phys. A **278**, 69 (1976).
[29] M. Muenchow and W. Scheid, Phys. Lett. B **162**, 265 (1985); Nucl. Phys. A **468**, 59 (1987).
[30] M. Rashdan, A. Faessler, and W. Wadia, J. Phys. G **17**, 1401 (1991).
[31] S. Kumar and R. K. Gupta, Phys. Rev. C **55**, 218 (1997).
[32] H. S. Khosla, S. S. Malik, and R. K. Gupta, Nucl. Phys. A **513**, 115 (1990).
[33] R. K. Gupta, S. Kumar, and W. Scheid, Int. J. Mod. Phys. E **6**, 259 (1997).
[34] K. Nishio *et al.*, Phys. Rev. C **82**, 024611 (2010).